Recent Results from ARGUS

H.Kapitza

Carleton University, Ottawa, Canada

(representing the ARGUS Collaboration*)

Abstract

Some recent results are reported from the ARGUS experiment, operated at the e^+e^- storage ring DORIS II at DESY. In an updated analysis of semileptonic $b \to u$ decays direct evidence for such transitions was obtained through reconstruction of a complete event. A study of the lepton energy spectra in $\tau^- \to e^-\nu\bar{\nu}$ and $\tau^- \to \mu^-\nu\bar{\nu}$ decays yielded a value for the Michel parameter which is in good agreement with a standard $V-A$ coupling at the τ-ν_τ-W vertex. A parity violating asymmetry was measured in τ decays into three charged pions which shows that the τ neutrino has negative helicity. The Micro Vertex Drift Chamber was installed as a new hardware component of the ARGUS detector. Initial results concerning backgrounds and chamber performance are presented.

1 Introduction

The results reported here were obtained using data collected with the ARGUS detector at the e^+e^- storage ring DORIS II. During the period 1983 to 1989 an integrated luminosity of $455\,\mathrm{pb}^{-1}$ was accumulated at center-of-mass energies between 9.4 and 10.6 GeV. About one half of this data sample ($237\,\mathrm{pb}^{-1}$) was taken on the $\Upsilon(4S)$ resonance and contains about 202 000 $\Upsilon(4S)$ decays. In order to determine the contributions from the continuum underlying the $\Upsilon(4S)$, data corresponding to a luminosity of $98\,\mathrm{pb}^{-1}$ were recorded at center-of-mass energies about 100 MeV below the $\Upsilon(4S)$ mass.

The ARGUS detector and its particle identification capabilities have been described in detail elsewhere [1]. The identification of leptons is of particular importance for two of the analyses presented here. At ARGUS this is done by combining available information from several detector components into a global likelihood ratio. For electrons, this likelihood ratio is constructed from

measurements of the energy deposition, the size and lateral spread of the associated cluster in the electromagnetic calorimeter, specific ionization in the main drift chamber, and time-of-flight. For muons, the quality of the match between the projected particle track and the associated hit in the muon chambers, located outside the magnet return yoke, is also used in forming the likelihood ratio. A particle is considered to be an electron or a muon if the corresponding likelihood ratio exceeds 0.8. This approach leads to a high efficiency of lepton identification, combined with a low misidentification rate for hadrons [1].

2 Analysis of Semileptonic $b \to u$ Decays

In the Standard Model with three families of quarks and leptons the b quark is allowed to decay weakly into a c or a u quark. The decay strengths are determined by the Cabibbo-Kobayashi-Maskawa (CKM) matrix elements V_{cb} and V_{ub} respectively. The copious production of charmed hadrons in B meson decays demonstrates that $b \to c$ transitions are strongly dominant [2]. On the other hand, a non-zero value of the CKM matrix element V_{ub} is essential for the explanation of CP violation in the Standard Model [3].

Among the various approaches to measure $b \to u$ transitions the analysis of charmless semileptonic B meson decays offers several advantages. Since these decays proceed only through the spectator diagram shown in Figure 1, their measurement provides the most reliable means of determining V_{ub}. Experimentally there is a simple kinematic separation of semileptonic $b \to u$ from $b \to c$ decays possible. Due to the mass difference of the lightest charmed hadrons $(D^{\pm}, D^0)$ and the lightest non-charmed hadrons $(\pi^{\pm}, \pi^0)$ the maximum lepton momentum is larger for $b \to u$ than for $b \to c$ transitions. In the rest system of the decaying B meson the kinematic limits are $p_{\ell,max} = 2.31\ (2.64)\,\mathrm{GeV}/c$ for $b \to c$ $(b \to u)$ decays. Hence searching for semileptonic $b \to u$ decays

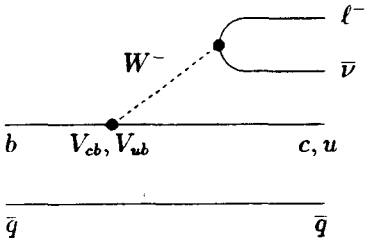

Figure 1: Spectator diagram for semileptonic B decays.

means looking for leptons with momenta beyond the kinematic limit for $b \to c$ transitions. This approach of measuring $b \to u$ transitions has been successful recently [4,5]. In the following an update of the published ARGUS analysis [5] is presented.

2.1 Inclusive Lepton Momentum Spectrum

The detailed event selection criteria can be found in [5], and only the general analysis ideas and new cuts will be described here. The basic requirement is to have at least one identified lepton in the event (see Section 1). However, most of the leptons in the $b \to u$ signal region are background, namely

- leptons from the continuum,
- leptons from $b \to c$ transitions,
- leptons from $B \to J/\psi X$, followed by $J/\psi \to \ell^+\ell^-$,
- misidentified hadrons.

These backgrounds can be substantially reduced by requiring a large missing momentum, $1.0 < p_{miss} < 3.5\,\mathrm{GeV}/c$, in the events. This cut is motivated by the presence of an energetic neutrino in the decay $B \to X_u \ell^- \bar{\nu}$[1]. It is very effective since continuum leptons, leptons from J/ψ decays, and misidentified hadrons are usually not accompanied by neutrinos.

In order to reduce the background further, two independent data samples were defined:

1. Events with exactly two leptons: Requiring an additional lepton with a momentum in the $b \to c$ range $1.2 < p_\ell < 2.3\,\mathrm{GeV}/c$ yields an almost background free sample of events. Residual lepton pairs from the continuum, converted photons, and J/ψ decays are suppressed by opening angle and invariant mass cuts.

2. Events with exactly one lepton: Here additional cuts must be applied on event topology and missing momentum. The former exploits the fact that particles from $\Upsilon(4S)$ decays are isotropically distributed while continuum events show a two-jet structure.

In the published analysis [5] the topology cut was implemented by demanding a large scalar sum of momentum ($> 2\,\mathrm{GeV}/c$) transverse to the lepton in a restricted angular region (60° to 120°) perpendicular to the lepton direction. The neutrino and charged lepton were forced to be back-to-back by requiring the angle β between the lepton and missing momentum direction to satisfy $\cos\beta < -0.5$.

[1] References in this paper to a specific charged state should be interpreted as also implying the charge conjugate state.

In order to enlarge the available single-lepton sample further, an alternative analysis has been devised which increases the overall acceptance for $b \to u$ leptons. This is achieved by first replacing the topological cut by the requirement that the cosine of the angle α between the direction of the lepton and the thrust axis of the rest of the event satisfies $|\cos\alpha| < 0.75$. As shown in Figure 2, continuum events are strongly peaked near $|\cos\alpha| = 1$, reflecting the two-jet topology of these events, in contrast to the flat distribution of $\Upsilon(4S)$ events. Secondly, the requirement that the lepton and the missing momentum be back-to-back, was replaced by a restriction that the squared mass of the hadronic system recoiling against the lepton and missing momentum,

$$M_h^2 \approx [E_{beam} - E_\ell - p_{miss}]^2 - [\vec{p}_\ell + \vec{p}_{miss}]^2 ,$$

must satisfy $|M_h^2| < 1.5\,\mathrm{GeV}^2/c^4$. This essentially is a cut against charmed hadronic systems. Monte Carlo studies show that about 55 % of the events which pass either the original or the modified cuts, should actually satisfy both. This is in good agreement with the observed overlap in the data.

In the $b \to u$ signal region of the lepton momentum spectrum, $2.3 < p_\ell < 2.6\,\mathrm{GeV/c}$, for events which satisfy either the original or the revised selection criteria, 109 leptons are observed in the $\Upsilon(4S)$ data (see Table 1). In order to obtain the number of leptons from direct $\Upsilon(4S)$ decays the continuum contribution has to be subtracted. A scaling factor of 2.42 takes into account the different luminosities and center-of-mass energies for continuum and $\Upsilon(4S)$ data. Contributions from the tail of the $b \to c$ spectrum are small. The same is true for the backgrounds from faked leptons and from J/ψ decays.

An updated analysis of the dilepton events results in 23 events having a lepton with momentum between 2.3 and 2.6 GeV/c. Only few of these are

	Single Leptons		Dileptons	
	e	μ	e	μ
$\Upsilon(4S)$	52	57	12	11
Backgrounds:				
Continuum (scaled)	10.7	19.9	0.8	0.8
$b \to c$	5.5	6.3	1.2	1.3
J/ψ	1.0	0.7	0.2	0.1
Fakes	1.3	2.8	0.8	1.5
Total background	18.5 ± 3.1	29.7 ± 4.3	3.0 ± 1.0	3.7 ± 0.9
Signal	33.5 ± 7.8	27.3 ± 8.7	9.0 ± 3.6	7.3 ± 3.4
Combined signal	77.1 ± 13.4			

Table 1: Observed numbers of single-lepton and dilepton events in the momentum interval $2.3 < p_\ell < 2.6\,\mathrm{GeV/c}$ and estimated backgrounds.

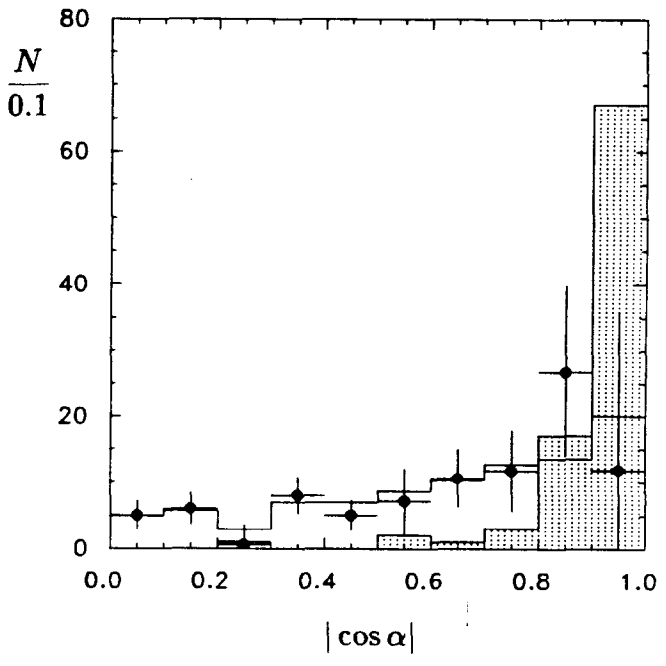

Figure 2: Distribution of $\cos\alpha$ for direct $\Upsilon(4S)$ decays (points with error bars), continuum events (shaded histogram, before scaling), and Monte Carlo generated $\Upsilon(4S)$ events where one B decays via $\overline{B}^0 \to \rho^0 \ell^- \bar{\nu}$ (open histogram, normalized to the direct $\Upsilon(4S)$ data). α is the angle between the direction of the lepton and the thrust axis of the rest of the event.

background, see Table 1. Figure 3 shows the lepton momentum spectrum of the combined single-lepton and dilepton samples. There remains, after subtraction of all backgrounds, a combined signal of 77.1 ± 13.4 events containing a lepton with $2.3 < p_\ell < 2.6\,\mathrm{GeV/c}$. The shape of the spectrum in this interval is compatible with the predictions for semileptonic $b \to u\ell^-\bar{\nu}$ decays [6,7,8,9]. However, using only this restricted portion of the full momentum spectrum, it is not possible to discriminate between the available models. Events containing electrons or muons contribute about the same number of events to the signal, as expected from their similar acceptances. The observed lepton rate in the $b \to u$ signal region can be compared to the lepton rate from $\Upsilon(4S)$ decays in the momentum range $2.0 < p_\ell < 2.3\,\mathrm{GeV/c}$:

$$\frac{\mathrm{BR}(B \to X\ell^-\bar{\nu},\ 2.3 < p_\ell < 2.6\,\mathrm{GeV/c})}{\mathrm{BR}(B \to X\ell^-\bar{\nu},\ 2.0 < p_\ell < 2.3\,\mathrm{GeV/c})} = (5.4 \pm 0.9)\%.$$

From this result the ratio $|V_{ub}/V_{cb}|$ can be calculated, using model predictions for the semileptonic decay rates and lepton momentum spectra in $b \to u\ell^-\bar{\nu}$ and $b \to c\ell^-\bar{\nu}$ decays. The results are shown in Table 2. The uncertainty due to the model dependence is of the same order as the experimental errors.

model	reference	$\lvert V_{ub}/V_{cb}\rvert$
ACM	[6]	0.11 ± 0.01
WBS	[7]	0.13 ± 0.02
KS	[8]	0.10 ± 0.01
GISW	[9]	0.19 ± 0.03

Table 2: $|V_{ub}/V_{cb}|$ for different models.

2.2 Reconstruction of $b \to u$ Events

In order to show that the observed excess of leptons in the momentum range $2.3 < p_\ell < 2.6\,\mathrm{GeV/c}$ does indeed originate from $b \to u$ transitions, an attempt was made to completely reconstruct the signal events. Monte Carlo studies and previous experience with tagging hadronic B decays in the data show that the reconstruction rate using all B decay channels involving D mesons[2] is about 1.6 % [10]. Therefore approximately one complete event is anticipated in the combined single-lepton sample.

As a result of the search for a hadronic B tag in the mentioned decay modes, one fully reconstructed event was found in the data, consistent with the expectation. The event is shown in Figure 4, and consists of a $\Upsilon(4S)$ decay into a pair

[2]Here D meson should be interpreted as D^0, D^+, D^{*0}, D^{*+} and their charge conjugate states. The final state of the B decay was required to contain no more than eight charged particles and six photons.

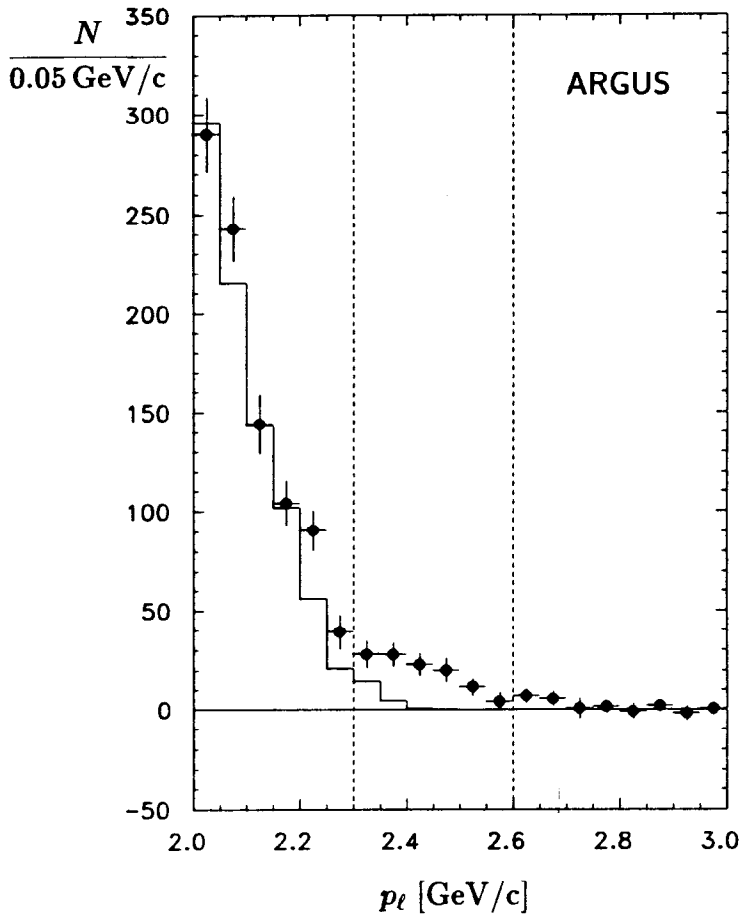

Figure 3: Combined lepton momentum spectrum for direct $\Upsilon(4S)$ decays. The histogram is the $b \to c$ contribution normalized in the region 2.0 - 2.3 GeV/c.

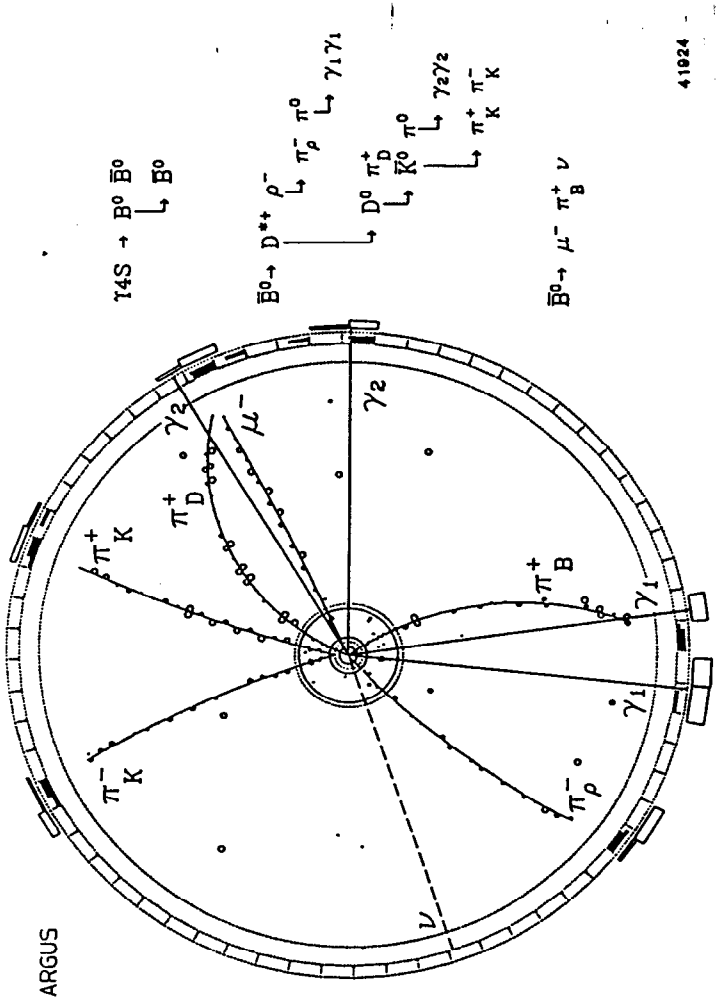

Figure 4: Completely reconstructed event containing a decay $\Upsilon(4S) \to B^0\overline{B}^0$, $B^0 \to \overline{B}^0$, where one $\overline{B}^0$ decays into $\pi^+\mu^-\overline{\nu}$ and the other into $D^{*+}\rho^-$.

of $\overline{B}^0$ mesons, indicating that one B^0 meson has oscillated into a $\overline{B}^0$. Thus the event simultaneously demonstrates the existence of $b \to u$ transitions and $B^0\overline{B}^0$ mixing. The hadronic $\overline{B}^0$ tag was reconstructed in the mode $\overline{B}^0 \to D^{*+}\rho^-$. The second $\overline{B}^0$ meson was seen in the channel $\overline{B}^0 \to \pi^+\mu^-\overline{\nu}$, representing the first direct observation of a $b \to u$ decay. The relevant kinematic quantities for this event are listed in Table 3. All measured intermediate masses agree well with the expected values [11].

$\Upsilon(4S) \to B^0\overline{B}^0, B^0 \to \overline{B}^0$			
	p [GeV/c]	M [MeV/c^2]	$\cos\theta$
$\overline{B}^0 \to \pi_B^+\mu^-\overline{\nu}$			
π_B^+	0.213 ± 0.003		-0.423
μ^-	2.322 ± 0.026		0.205
$\overline{\nu}$	2.667 ± 0.034		-0.130
$\overline{B}^0 \to D^{*+}\rho^-$	0.330 ± 0.021	5277.7 ± 3.3	-0.12
$D^{*+} \to \pi_D^+ D^0$	2.278 ± 0.013	2010.0 ± 1.0	-0.62
π_D^+	0.204 ± 0.005		-0.72
$D^0 \to \pi^0\overline{K}^0$	2.074 ± 0.014	1767 ± 62	-0.61
$\pi^0 \to \gamma_2\gamma_2$	0.602 ± 0.045	114 ± 17	0.27
$\overline{K}^0 \to \pi_K^+\pi_K^-$	2.041 ± 0.010	494.2 ± 4.1	-0.70
$\rho^- \to \pi_\rho^-\pi^0$	2.002 ± 0.159	747 ± 33	0.64
π_ρ^-	0.598 ± 0.003		0.43
$\pi^0 \to \gamma_1\gamma_1$	1.518 ± 0.160	127 ± 22	0.69

Table 3: Kinematic quantities of the event in Figure 4.

Possible background sources to this event have been evaluated. The probability for misinterpretation is substantially reduced by the existence of a D^{*+} in the event. Also of particular importance is the fact that the missing momentum $p_{miss} = (2.667 \pm 0.034)$ GeV/c coincides within errors with the missing energy $E_{miss} = (2.711 \pm 0.027)$ GeV. Since the missing momentum vector points into the barrel region of the detector, where no interaction is observed, the missing particle is most probably a neutrino. The μ^- is well measured, with hits in all three layers of the muon chambers. If the muon were actually faked by a hadron, the missing particle could also be a non-interacting K_L^0. However, this hypothesis is ruled out for most $b \to c$ decays, since such a hypothetical, high momentum K_L^0 would be beyond the kinematic limit for all but a sequence of two-body decays. Since the invariant mass formed by a missing K_L^0 with either the soft pion or the muon lies outside the charmed hadron region, the two-body decay hypotheses can be safely rejected. The possibility that this decay proceeds via a "penguin" diagram in the channel $B^0 \to K_L^0\pi^-\pi^+$ cannot

be excluded, but has a probability of less than 10^{-3} due to the smallness of the lepton fake rate and the "penguin" decay rate [12]. Misreconstruction of a continuum process is also very unlikely, with a probability estimated to be less than 10^{-3} by measuring the fake rate for hadronic B tags in the continuum data.

Therefore the most probable interpretation of this event is that a completely reconstructed $\Upsilon(4S)$ decay was observed, where one $\overline{B}^0$ meson decays into $\pi^+\mu^-\overline{\nu}$. This represents the first direct observation of a $b \to u$ transition.

3 Determination of the Michel Parameter in τ Decays

All experimental studies of the space-time structure of weak charged currents are in agreement with the existence of a universal $V-A$ interaction, as assumed in the Standard Model. This has been shown with high precision for the decay of the muon, $\mu^- \to e^-\overline{\nu}_e\nu_\mu$, by comparing the shape of the electron energy spectrum with theoretical predictions. The electron energy spectrum in the muon rest frame is given by the one-parameter Michel formula [13]

$$\frac{dN}{dx} \propto x^2[12(1-x) - \frac{8}{3}\rho(3-4x) + r(x)],$$

where x is the lepton energy divided by its maximum kinematically allowed value. For a $V-A$ coupling at the muon decay vertex a Michel parameter $\rho = 0.75$ is expected. All other linear combinations of V and A couplings lead to values $\rho < 0.75$, in particular $\rho = 0$ for $V+A$ and $\rho = 0.375$ for pure V or pure A. A measurement of $\rho > 0.75$ would indicate the presence of scalar and tensor couplings. The radiative correction term $r(x)$ is not negligible and depends on the assumed combination of V and A couplings.

In muon decay the Michel parameter has been measured with high precision, and the average result, $\rho = 0.7518 \pm 0.0026$ [11], is in excellent agreement with the $V-A$ theory. Assuming e-μ-τ universality, the same is expected to hold true for leptonic tau decays (Figure 5). This assumption, however, is not well tested experimentally. Although the world average for the Michel parameter measured in τ decays is in reasonable agreement with the $V-A$ theory, there is a large spread between individual measurements (see Table 4). Moreover, the values of ρ extracted from electron spectra differ by about two standard deviations from those obtained from muon spectra.

Using the full available data sample of $455\,\mathrm{pb}^{-1}$ and exploiting the good lepton identification capabilities, a high-precision measurement of the Michel parameter in the decays $\tau^- \to e^-\nu\overline{\nu}$ and $\tau^- \to \mu^-\nu\overline{\nu}$ has been performed at ARGUS [18]. The experimental electron and muon energy spectra are obtained

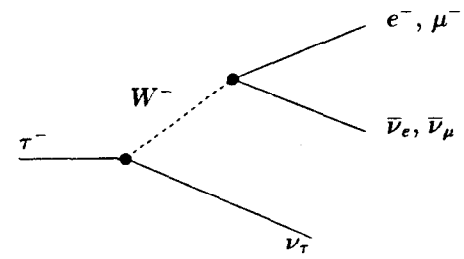

Figure 5: Feynman diagram for leptonic τ decays.

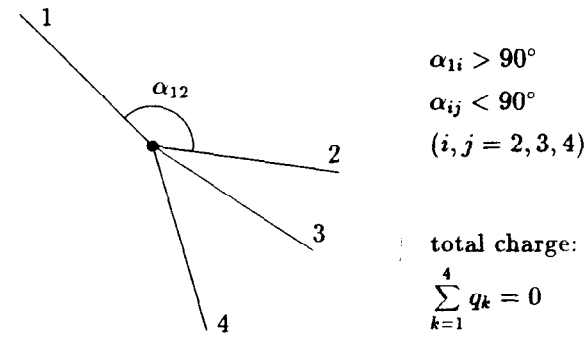

Figure 6: Selected one-versus-three event topology.

Experiment	$\tau^- \to e^-\nu\bar{\nu}$	$\tau^- \to \mu^-\nu\bar{\nu}$	Average
DELCO [14]	0.72 ± 0.15		0.72 ± 0.15
CLEO [15]	0.60 ± 0.13	0.81 ± 0.13	$0.71 \pm 0.09 \pm 0.03$
MAC [16]	$0.62 \pm 0.17 \pm 0.14$	$0.89 \pm 0.14 \pm 0.08$	$0.79 \pm 0.10 \pm 0.10$
CB [17]	$0.64 \pm 0.06 \pm 0.07$		$0.64 \pm 0.06 \pm 0.07$
Average	0.64 ± 0.06	0.84 ± 0.11	0.70 ± 0.05

Table 4: Previous measurements of the Michel parameter in the decays $\tau^- \to e^-\nu\bar{\nu}$ and $\tau^- \to \mu^-\nu\bar{\nu}$.

from a sample of tau-pair events where one τ decays into three charged particles and the other into one identified lepton:

$$e^+e^- \to \tau^+\tau^- \to \nu_\tau e^-\bar{\nu}_e, \nu_\tau\mu^-\bar{\nu}_\mu$$
$$\hookrightarrow \bar{\nu}_\tau\pi^+\pi^+\pi^-(\pi^0)\,.$$

The required one-versus-three event topology is defined in Figure 6. In order to assure good momentum resolution and trigger conditions, the single track must point into the barrel region of the detector, restricting its polar angle to the region $|\cos\theta| < 0.75$. There should be no more than three photons with $E_\gamma > 80\,\mathrm{MeV}$ in the shower counters, thereby allowing for the possibility of one radiative photon in addition to the π^0 from the decay $\tau^+ \to \bar{\nu}_\tau\pi^+\pi^+\pi^-\pi^0$.

Some further cuts were applied in order to suppress backgrounds from the following sources:

1. Radiative Bhabha and muon pair events with one photon converting into an e^+e^- pair close to the interaction point, are characterized by small total transverse momentum $P_T = |\sum \vec{p}_T|$ and high visible energy E_{tot}. This background was suppressed by requiring $P_T > 0.3\,\mathrm{GeV/c}$. The energy deposited in the electromagnetic calorimeter by all charged particles on the three-prong side was required to be less than 3.5 GeV. The angle $\alpha_\pm$ between oppositely charged particles on the three-prong side had to satisfy the condition $\cos\alpha_\pm < 0.992$.

2. Events from two-photon interactions with the initial e^- (e^+) tagged in the detector have a missing momentum vector $\vec{p}_{miss}$ which points along the direction of the e^+ (e^-) which escaped down the beam pipe. This background is relevant only for $\tau^- \to e^-\nu\bar{\nu}$ decays, and was eliminated by a requirement on the direction of the missing momentum, $q_e \times \cos\theta_{miss} \geq -0.95$, where q_e is the charge of the tagged $e^\pm$.

3. Two-photon events without an electron tag may contain a faked lepton. These events are characterized by small E_{tot} and P_T, since both initial electron and positron are not detected. This background is practically eliminated by the P_T cut.

4. Contributions from the hadronic one-prong tau decay $\tau^- \to \rho^-\nu_\tau$, followed by $\rho^- \to \pi^-\pi^0$ and $\pi^0 \to \gamma\gamma$ were removed by allowing no more than one photon on the one-prong side, and restricting the energy of that photon to a maximum of 300 MeV.

A sample of 5106 events containing electrons and 3041 events containing muons satisfied these selection criteria. The remaining background is summarized in Table 5. The multihadron background was estimated from the distribution of the invariant mass $M(3\pi)$ on the three-prong side. There are only 11 events observed with a mass higher than M_τ which have been rejected for the further analysis. The background from the decay $\tau^- \to \pi^-\nu_\tau$ was determined using the known pion-lepton misidentification rates [1]. The background from the decay $\tau^- \to \mu^-\nu\bar{\nu}$ in the electron channel occurs mainly at momenta below $1\,\mathrm{GeV/c}$ where muons can fake electrons.

Background	$\tau^- \to e^-\nu\bar{\nu}$	$\tau^- \to \mu^-\nu\bar{\nu}$
multihadron events radiative QED events two-photon events	0.3	0.3
$\tau^- \to \pi^-\nu_\tau$	0.3	1.5
$\tau^- \to \rho^-\nu_\tau$	-	0.2
$\tau^- \to \mu^-\bar{\nu}_\mu\nu_\tau$	0.2	-
Total	0.8	2.0

Table 5: Remaining backgrounds (in %) in the $\tau^- \to e^-\nu\bar{\nu}$ and $\tau^- \to \mu^-\nu\bar{\nu}$ data samples.

Knowledge of the lepton identification efficiency is of particular importance for this analysis, since any momentum dependence would distort the shape of the energy spectrum. Therefore a detailed study of the lepton identification efficiency was performed using experimental data. Radiative Bhabha events were used as a clean sample of electrons. A comparison of efficiencies determined from experimental data and by Monte Carlo simulation is shown in Figure 7a. In order to determine the muon identification efficiency over a wide momentum range, cosmic ray events were analyzed. Again, the Monte Carlo results agree well with the data over the whole momentum range, as shown in Figure 7b. The large values of electron and muon identification efficiencies and their weak momentum dependence allow a measurement of the Michel parameter with a small systematic uncertainty.

The electron and muon x-distributions are shown in Figure 8 together with the radiatively corrected theoretical spectra [19]. The data strongly favour the

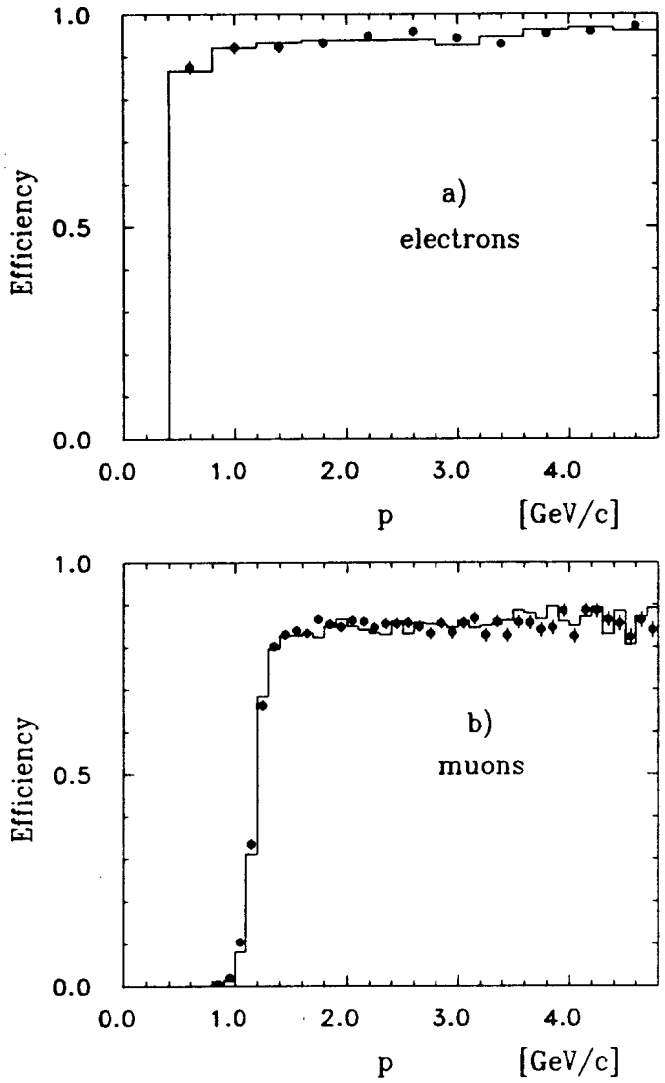

Figure 7: Efficiency of (a) electron and (b) muon identification determined from experimental data (points) and Monte Carlo simulation (histogram).

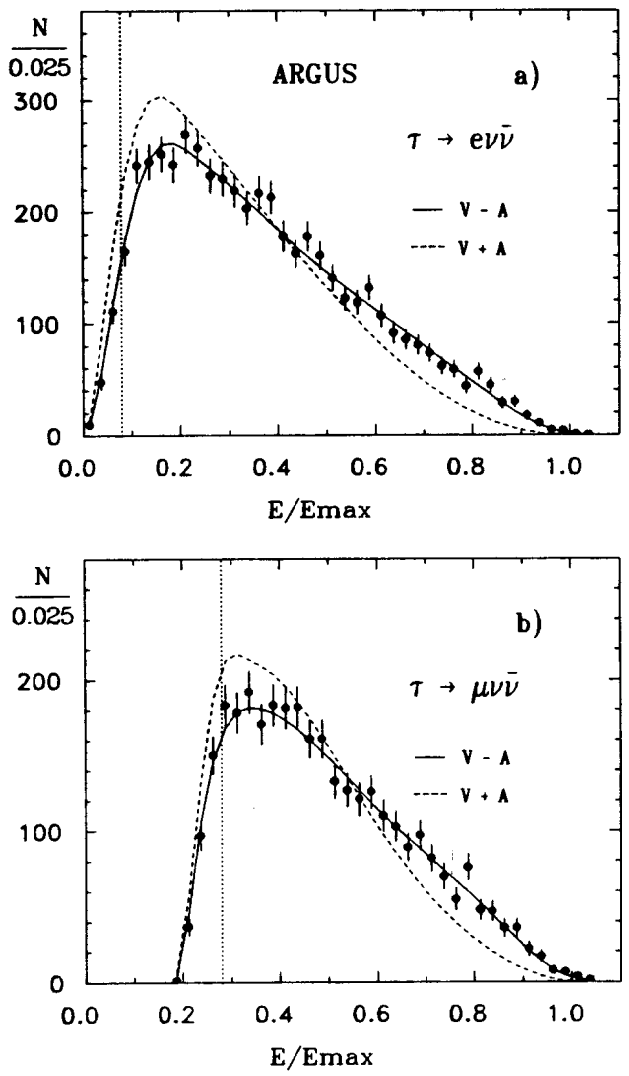

Figure 8: Normalized (a) electron and (b) muon energy spectra from leptonic τ decays compared with the $V-A$ (solid line) and $V+A$ (dashed line) predictions.

$V-A$ spectrum. The further analysis was restricted to the region of reliable lepton identification, corresponding to $x > 0.08$ for electrons and $x > 0.28$ for muons. These boundaries are indicated by the vertical lines in the figure. After subtraction of the background the experimental distributions were fitted with a theoretical model with an arbitrary parameter ρ. The results of the fits are

$$\rho = \begin{cases} 0.747 \pm 0.045 \pm 0.028 & \text{for electrons} \\ 0.734 \pm 0.055 \pm 0.027 & \text{for muons} \\ 0.742 \pm 0.035 \pm 0.020 & \text{weighted average.} \end{cases}$$

The measurements for electrons and muons are clearly in good agreement. The different sources of systematic error have been analyzed in detail. The main contribution for electrons comes from the uncertainties in the lepton identification and trigger efficiencies. For muons, the dominant uncertainty is due to the background from $\tau^- \to \pi^- \nu_\tau$ decays.

The ARGUS measurement represents a considerable improvement both in terms of statistical and systematic error (see Table 4). The measured value of the Michel parameter is in good agreement with the $V-A$ theory and excludes both $V+A$ and pure V or A couplings at the τ-ν_τ-W vertex as long as the electron and muon vertices have the standard $V-A$ structure. This result provides further confirmation of e-μ-τ universality.

4 Determination of the τ Neutrino Helicity

A completely different and more direct approach of checking the $V-A$ nature of weak charged currents in τ decays is to measure the helicity of the τ neutrino. For a pure $V-A$ interaction, as implemented in the Standard Model, massless neutrinos are strictly left-handed. A definite helicity of the ν_τ imposes restrictions on the possible spin orientations of a vector particle X^- in the decay $\tau^- \to X^- \nu_\tau$, as schematically shown in Figure 9. A unique ν_τ helicity results in a sign asymmetry of $J_z(X^-)$. However, in most cases such an asymmetry remains unmeasurable because the sign of J_z is lost when squaring the decay amplitude.

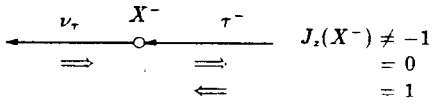

Figure 9: Possible spin orientations in the rest frame of the vector particle X^- for the decay $\tau^- \to X^- \nu_\tau$ and negative ν_τ helicity.

As pointed out by Kühn and Wagner [20] the situation is different in the decay

$$\tau^- \to a_1^-(1260)\,\nu_\tau \to \pi^+\pi^-\pi^-\nu_\tau \,.$$

Here the subsequent strong decay of the a_1^- can be used to analyze the ν_τ helicity. The $a_1^-(1260)$ is known to decay predominantly via an S-wave $\rho^0\pi^-$ intermediate state into three pions:

$$a_1^- \to \rho^0\pi^- \to \pi^+\pi_1^-\pi_2^- \,.$$

Due to its large width there are two possibilities to form a ρ^0 from the observed final state particles ($\pi^+\pi_1^-$ and $\pi^+\pi_2^-$) and the corresponding amplitudes must be added coherently (Figure 10). Because of the interference term the squared decay matrix element still contains information about the sign of $J_z(a_1^-)$ and hence is sensitive to the ν_τ helicity.

Details about the calculation of the decay matrix element can be found in [20,21], and only the relevant features of the final result will be presented here. In the following q_1, q_2, q_+ and $Q = q_1 + q_2 + q_+$ denote the four-momenta of the pions π_1^-, π_2^-, π^+ and of the three-pion system. From these vectors one can construct the two-pion invariant masses $s_{1,2} = (q_{2,1} + q_+)^2$. The squared decay matrix element in the three-pion rest frame consists of a parity conserving and a parity violating part:

$$\omega = \omega_{PC} + \omega_{PV} \,.$$

For the parity violating part one finds

$$\omega_{PV} \propto \pm\, \gamma_{AV}\, \vec{p}_0 \cdot \vec{n}_0\, (s_1 - s_2) \,,$$

where only the factors related to parity violation are shown. The '$\pm$' denotes the sign of the charge of the decaying τ. The vectors $\vec{p}_0$ and $\vec{n}_0$ are the τ momentum unit vector and the normal unit vector on the three-pion plane respectively, both defined in the three-pion rest frame (see Figure 11). The axial vector

$$\vec{n}_0 = \frac{\vec{q}_1 \times \vec{q}_2}{|\vec{q}_1 \times \vec{q}_2|}$$

introduces an orientation of the three-pion plane. This definition makes sure that ω_{PV} is invariant under the exchange of the two identical particles π_1^- and π_2^- because the expression $\vec{n}_0\,(s_1 - s_2)$ does not change sign. A uniquely defined orientation of the three-pion plane is given by $\vec{n}_0 \cdot \mathrm{sign}(s_1 - s_2)$ which implies an ordering of the particles π_1^- and π_2^- according to their momentum. The axial vector $\vec{n}_0 \cdot \mathrm{sign}(s_1 - s_2)$ carries information about the spin of the ν_τ while the vector $\vec{p}_0$ describes the ν_τ momentum. If the average value of the pseudoscalar $\vec{p}_0 \cdot \vec{n}_0 \cdot \mathrm{sign}(s_1 - s_2)$ is measured to be different from zero, this is a clear indication of a preferred ν_τ helicity and hence of parity violation in τ decays. This

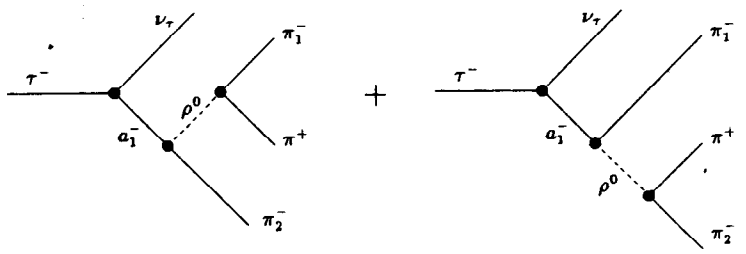

Figure 10: Interfering amplitudes for the a_1^- decay.

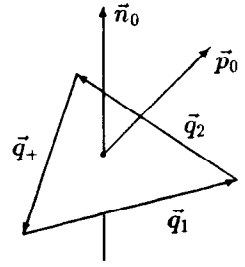

Figure 11: Unit vectors $\vec{p}_0$ and $\vec{n}_0$ in the decay $\tau^- \to \pi^+\pi^-\pi^-\nu_\tau$.

asymmetry is proportional to the normalized product of the weak vector and axial vector coupling constants

$$\gamma_{AV} = \frac{2\,C_A C_V}{C_A^2 + C_V^2}\,.$$

Here the sign convention $C_A = \pm C_V = \pm 1$, i.e., $\gamma_{AV} = \pm 1$, for a pure $V \mp A$ interaction is used.

The experimental determination of the asymmetry is complicated by the fact that the τ direction $\vec{p}_0$ is not observable. However, for τ's decaying in flight one can approximate it by $-\vec{Q}_0$, where $\vec{Q}_0$ is the boost direction of the three-pion system in the laboratory frame. The τ momentum lies on a cone around $-\vec{Q}_0$, see Figure 12. The opening angle is 2ψ where ψ can be calculated from measurable kinematic quantities [20]:

$$\cos\psi = -\vec{Q}_0 \cdot \vec{p}_0 = \frac{x(m_\tau^2 + Q^2) - 2Q^2}{(m_\tau^2 - Q^2)\sqrt{x^2 - 4Q^2/s}}\,.$$

Here $\sqrt{s}$ is the e^+e^- center-of-mass energy and $x = E_{3\pi}/E_{beam}$ the normalized hadronic energy in the laboratory frame. Replacing $\vec{p}_0 \cdot \vec{n}_0$ by $-\vec{Q}_0 \cdot \vec{n}_0$ means averaging over the unknown azimuthal angle ϕ:

$$-\vec{Q}_0 \cdot \vec{n}_0 = \langle \vec{p}_0 \cdot \vec{n}_0 \rangle_\phi \cos\psi\,.$$

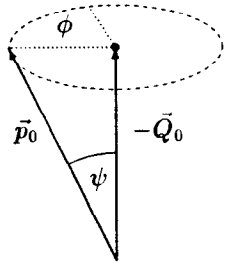

Figure 12: Relation between τ direction $\vec{p}_0$ and three-pion boost direction $-\vec{Q}_0$.

The quantity to be measured is the average value of the orientation of the three-pion plane with respect to $-\vec{Q}_0$ as a function of x and Q^2:

$$a(x, Q^2) \equiv \langle -\vec{Q}_0 \cdot \vec{n}_0 \cdot \mathrm{sign}(s_1 - s_2) \rangle = \mp \gamma_{AV} \cos\psi A(Q^2)\,.$$

The last part of this equation shows the expectation value of $-\vec{Q}_0 \cdot \vec{n}_0 \cdot \mathrm{sign}(s_1 - s_2)$ as calculated in the Kühn-Wagner model. The sign again indicates the charge of the decaying τ. The x dependence is fully contained in $\cos\psi$.

An experimental determination of the τ neutrino helicity and of γ_{AV} from a measurement of the asymmetry $A(Q^2)$ has been performed at ARGUS [22]. The analyzed data sample corresponds to an integrated luminosity of 264 pb^{-1}. The event selection follows an earlier analysis of the same final state [23]. Tau pair events from the reactions

$$e^+e^- \to \tau^+\tau^- \to \pi^+\pi^-\pi^-\nu_\tau$$
$$\hookrightarrow e^+\nu_e\bar{\nu}_\tau,\ \mu^+\nu_\mu\bar{\nu}_\tau,\ \pi^+\bar{\nu}_\tau,\ K^+\bar{\nu}_\tau,\ \rho^+\bar{\nu}_\tau$$

were selected by requiring a one-versus-three charged particle topology, similar to the one defined in Figure 6. In order to efficiently suppress the $\pi^+\pi^-\pi^-\pi^0\nu_\tau$ decay mode, photons with $E_\gamma \geq 80$ MeV were only allowed if they combined to exactly one π^0, which in combination with the single-prong forms a ρ^+ candidate with $0.54 < M(\pi^+\pi^0) < 1.0\,\mathrm{GeV/c^2}$ and an opening angle satisfying $\theta_{\pi^+\pi^0} < 53°$. Similar cuts as described in Section 3 were used to suppress radiative QED events. Background from two-photon and beam-gas events was suppressed by requiring a scalar momentum sum $2.7\,\mathrm{GeV/c} \leq \sum_{i=1}^{4} |\vec{p}_i| \leq 0.92\sqrt{s}$. Finally a cut on the angle ψ (see Figure 12) was applied, $\cos\psi > 0.2$. This cut reduces the background from multihadron and two-photon events. Although 35 % of all a_1^- candidates are rejected as well, the result of the analysis is not affected since around $\cos\psi = 0$ the measured quantity $a(x, Q^2)$ is not sensitive to the asymmetry $A(Q^2)$.

The cuts yield a sample of 3899 $\tau^+\tau^-$ events. The background contributions were determined from Monte Carlo simulations and are summarized in Table 6. The large systematic error on the background from other τ decay modes results from the uncertainties of their branching ratios.

Background	fraction [%]	asymmetry
other τ decay modes,		
in particular $\tau^- \to \pi^+\pi^-\pi^-\pi^0\nu_\tau$	$15.9 \pm 0.6 \pm 5.8$	0.010 ± 0.006
radiative QED events	1.00 ± 0.16	$(9 \pm 4) \cdot 10^{-5}$
multihadron events	0.72 ± 0.13	-
two-photon events	0.15 ± 0.06	-

Table 6: Fractions and asymmetries of the remaining backgrounds in the ν_τ helicity analysis.

Figure 13a shows the three-pion mass distribution of the selected events where 3887 events are τ candidates with $M(3\pi) < M_\tau$. The entries above the τ mass served to normalize the simulated multihadron background. The mass distribution of unlike-sign pion pair combinations (Figure 13b) shows a clear ρ peak with a combinatorial background which is approximately described by the like-sign combinations. Both the three-pion and two-pion mass spectra are in good agreement with an a_1 dominance in the three-pion final state.

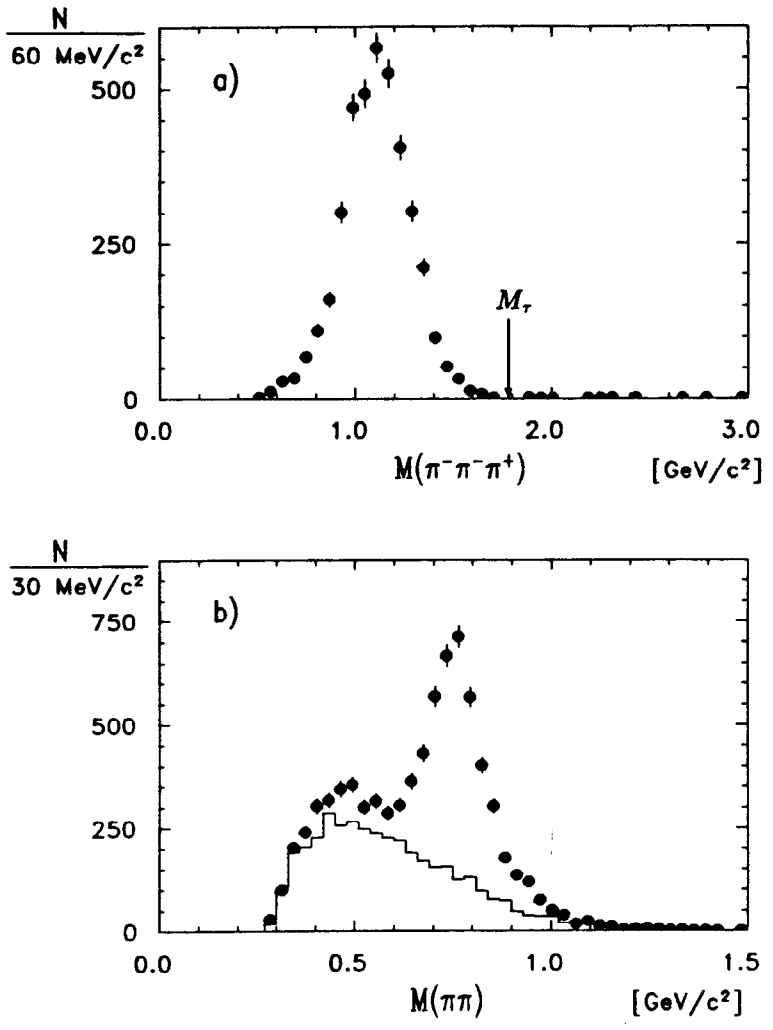

Figure 13: (a) Three-pion mass distribution for the decay $\tau^- \to \pi^+\pi^-\pi^-\nu_\tau$. (b) Two-pion mass distributions (points: $\pi^+\pi^-$ with two entries per event, histogram: $\pi^-\pi^-$).

The parity violating asymmetry $A(Q^2)$ for the selected τ candidates was determined in two steps. First the average values

$$a^{meas}(x,Q^2) = \langle -\vec{Q}_0 \cdot \vec{n}_0 \cdot \mathrm{sign}(s_1 - s_2) \rangle_{x,Q^2} \quad \text{and} \quad \langle \cos\psi \rangle_{x,Q^2}$$

were determined in (x, Q^2) bins of the size $\Delta x = 0.1$ and $\Delta Q^2 = 0.165\,\mathrm{GeV}^2/c^4$. Then the asymmetry $A(Q^2)$ was obtained by averaging over x:

$$A^{meas}(Q^2) = \left\langle \frac{a^{meas}(x,Q^2)}{\langle \cos\psi \rangle_{x,Q^2}} \right\rangle_x .$$

The measured asymmetries $A^{meas}(Q^2)$ are shown in Figures 14a and b for τ^- and τ^+ decays separately. The average asymmetries in the interval $0.7 < Q^2 < 2.0\,\mathrm{GeV}^2/c^4$ are

$$\langle A^{meas} \rangle = \begin{cases} -0.062 \pm 0.020 & \text{for } \tau^- \text{ decays,} \\ 0.060 \pm 0.019 & \text{for } \tau^+ \text{ decays.} \end{cases}$$

In both cases the experimentally determined asymmetries differ from zero by more than three standard deviations with signs as expected for a standard left-handed ν_τ.

The measured asymmetries must be corrected for the dilution due to the background. The asymmetries of the various background sources are listed in Table 6. The asymmetry of the background from $\tau^- \to \pi^+\pi^-\pi^-\pi^0\nu_\tau$ was determined from a sample of 1463 reconstructed decays where the π^0 was seen in the detector. Since the background contributions are found to have small asymmetries, the correction tends to increase the measured asymmetry. Figure 14c shows the combined background corrected asymmetry A^{exp} for τ^- and τ^+ as a function of Q^2. The τ^- asymmetry enters here with a reversed sign. The combined average result is

$$\langle A^{exp} \rangle = 0.063 \pm 0.016 .$$

This measurement establishes parity violation in the decay $\tau^- \to \pi^+\pi^-\pi^-\nu_\tau$ with a significance of four standard deviations, independently of any model.

In order to determine γ_{AV} quantitatively one writes

$$A^{exp}(Q^2) = \gamma_{AV}\, A^{calc}(Q^2) ,$$

where $A^{calc}(Q^2)$ is the acceptance corrected asymmetry function as calculated in the Kühn-Wagner model. This calculation includes a full simulation of the detector and of the selection efficiencies. At this stage it was also verified that detector effects cannot fake an asymmetry. A fit of $A^{calc}(Q^2)$ to the distribution shown in Figure 14c yields the result

$$\gamma_{AV} = \frac{2C_A C_V}{C_V^2 + C_A^2} = 1.14 \pm 0.34 \pm^{0.34}_{0.17} .$$

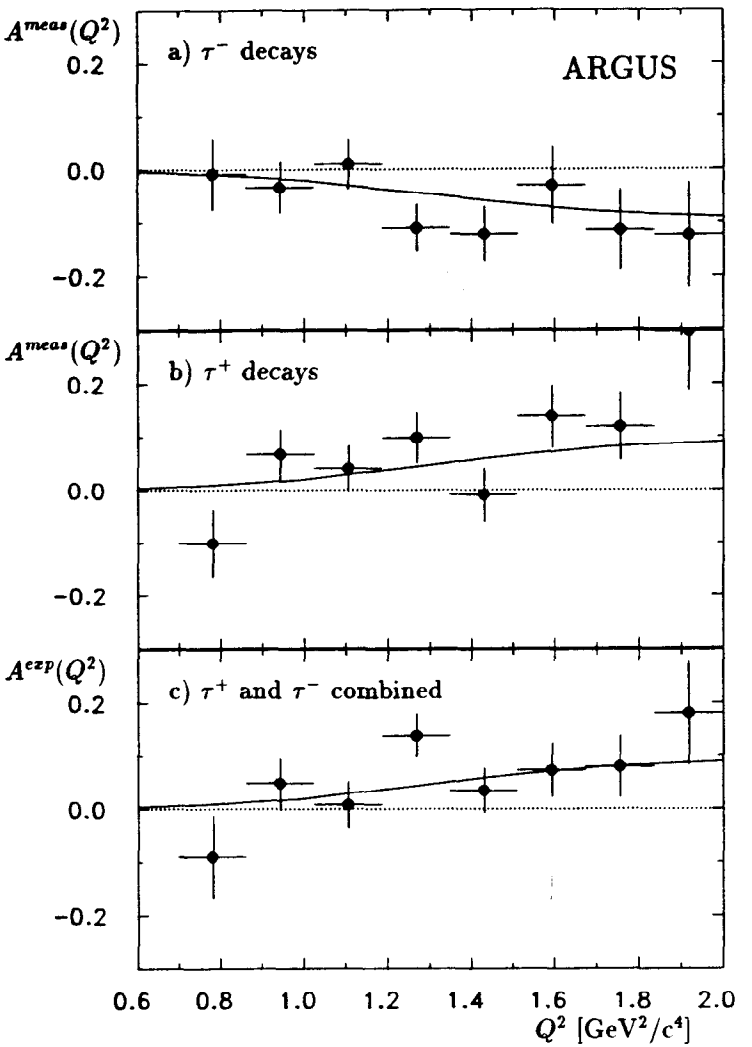

Figure 14: Measured asymmetry $A(Q^2)$ for (a) τ^- decays and (b) τ^+ decays. (c) Background corrected asymmetry $A^{exp}(Q^2)$ for τ^- and τ^+ decays combined. The solid lines show the asymmetry function $A(Q^2)$ as predicted by Kühn and Wagner, the dotted lines correspond to the case of no parity violation.

The systematic error is dominated by the theoretical uncertainty arising from the not well known D-wave contribution to the $a_1^- \to \rho^0\pi^-$ decay.

The result for γ_{AV} is consistent with the value expected for pure $V-A$ coupling at the τ-ν_τ vertex ($\gamma_{AV}=+1$). In the Kühn-Wagner model with only C_A and C_V as coupling constants this determines the ν_τ helicity to be negative.

5. Micro Vertex Drift Chamber Performance

In March 1990 the old ARGUS Vertex Drift Chamber [24] was replaced by the Micro Vertex Drift Chamber (μVDC) [25]. A data sample of about $15\,\mathrm{pb}^{-1}$ was accumulated on the $\Upsilon(4S)$ resonance and in the nearby continuum. First results concerning the chamber performance and background studies are presented here.

5.1 Chamber Design Summary

The μVDC is designed to resolve secondary vertices from the decays of short-lived particles like charmed mesons or tau leptons. The main design features can be summarized as follows:

- The chamber contains 1070 sense wires which are arranged in 16 layers, four layers of axial wires and six pairs of layers with wires at angles of $\pm 45°$ relative to the chamber axis. Due to these extremely large stereo angles the track coordinates in the r-ϕ and r-z projections can be measured with equal precision. On the other hand, the large stereo angles require a mechanical support structure for guiding the stereo wires around the chamber axis, as schematically shown in Figure 15.

- The inner chamber wall is a beryllium beam pipe with 19 mm outer radius and 0.5 mm wall thickness. These small dimensions and the low Z material help to keep the extrapolated track error at the beam position small.

- The innermost sense wire layer has a distance of only 26 mm from the beam line. It contains 35 drift cells which is about the minimum needed for a good multitrack resolution. These both constraints required the μVDC drift cells to be small (see Figure 16). All drift cells in the μVDC have the same size. The cathode design represents an optimum in terms of acceptable field strength on the wire surface and minimal multiple scattering.

- In small drift cells the achievable resolution is limited by ionization statistics. Hence the chamber must be operated at elevated pressure. The outer

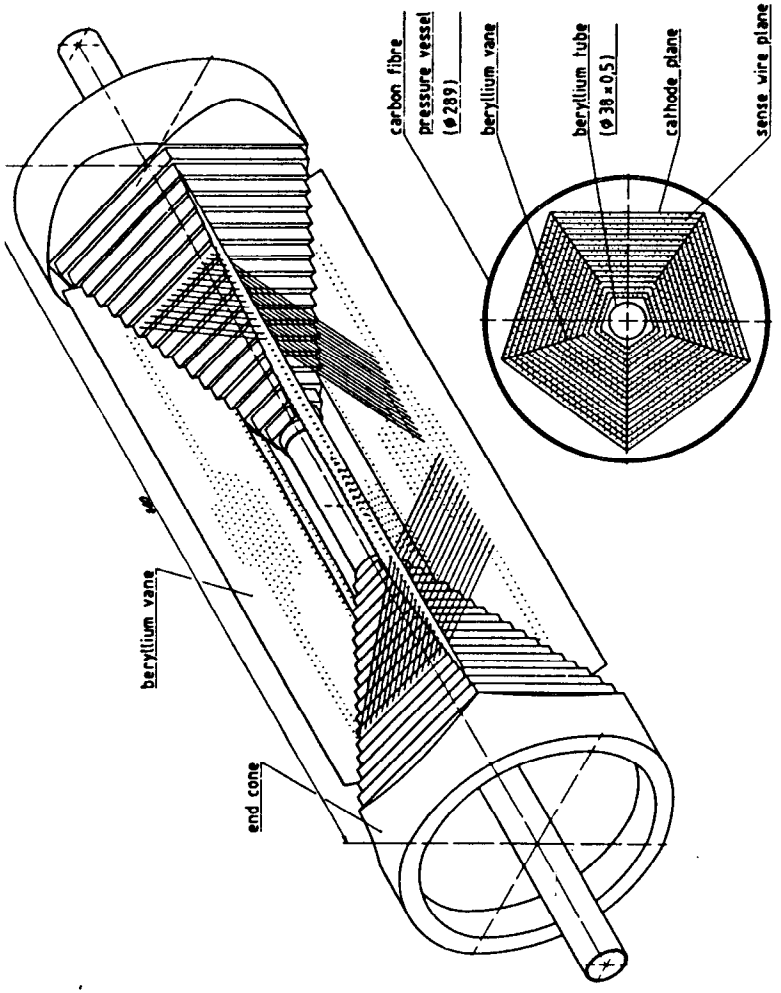

Figure 15: Schematic view of the μVDC. The stereo wires wrap around the chamber axis, supported by a structure made of five beryllium plates extending between two aluminium endcones. The wires are fed through jewels being inserted in the vanes (672 in each). The endcones carry ceramic boards on which the wires are accurately positioned and fixed.

chamber wall is a pressure vessel made of 2.2 mm thick carbon-fibre epoxy composite.

- Based on Monte Carlo simulations and test measurements, a scheme for synchrotron radiation shielding was developed, which makes operation of the μVDC close to the beam line possible. Additional dipole magnets were inserted on each side of the interaction region, splitting the last bend into two parts. As a result only radiation with a very low critical energy enters the interaction region. The direct radiation is screened by movable copper collimators on either side of the μVDC. Their backsides (towards the interaction point) are plated with titanium. The backscattered radiation from the titanium is attenuated by an 8 μm copper layer on the inner side of the beryllium beam pipe.

5.2 Chamber Operation

With an operating voltage of 3550 V two gas mixtures were used in the μVDC:

- pure CO_2 with a 0.3 % admixture of water at a pressure of 2.45 bar, and
- a mixture of 80 % CO_2 and 20 % propane with admixtures of methylal (3 %) and water (0.3 %) at a pressure of 3.1 bar.

In both cases the gas gain of the chamber was determined to be $A \approx 18000$. The electronics pulse height threshold was set to a current of 0.4 μA at the preamplifier input.

With the beam currents being less than 2×40 mA, the total μVDC current was less than 170 μA. From the mean operating conditions during the 48 days of data taking it was estimated that a charge of 80 mC/cm was collected on the wires of the innermost layer. It has been shown that chambers can be operated without aging problems up to several C/cm collected, provided that contaminants in the gas, in the tubing system, and in the chamber are avoided [26]. Hence, from the above estimate one would not expect any substantial aging of the μVDC yet. This is supported by the fact that at the end of data taking the total dark current of the chamber was still as low as 0.6 μA.

5.3 Chamber Resolution

Except for the region close to the sense wire the isochrones in the μVDC drift cell are strongly non-circular (see Figure 16). Hence the track angle must be taken into account when drift distances are calculated from the measured drift times. This angular correction was determined together with the space time relationship in an iterative calibration procedure using Bhabha events in the barrel

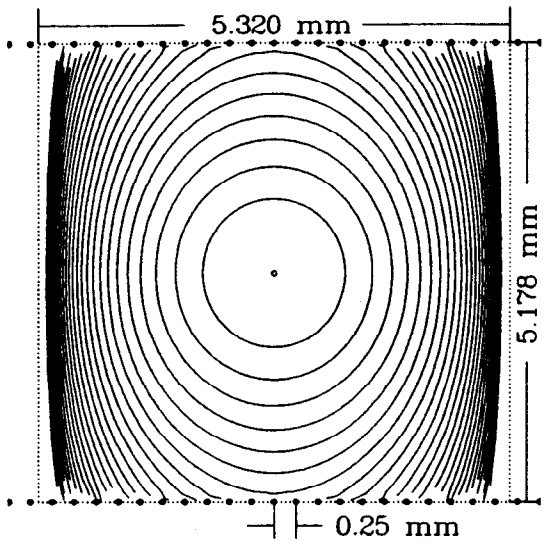

Figure 16: Design of the μVDC drift cell. Sense wire (open circle) and cathode wires (full circles) both have a diameter of 25 μm. Also shown are the isochrones for CO_2 at $p = 2.45$ bar and $HV = 3550$ V for drift times of 20 – 520 ns in steps of 20 ns.

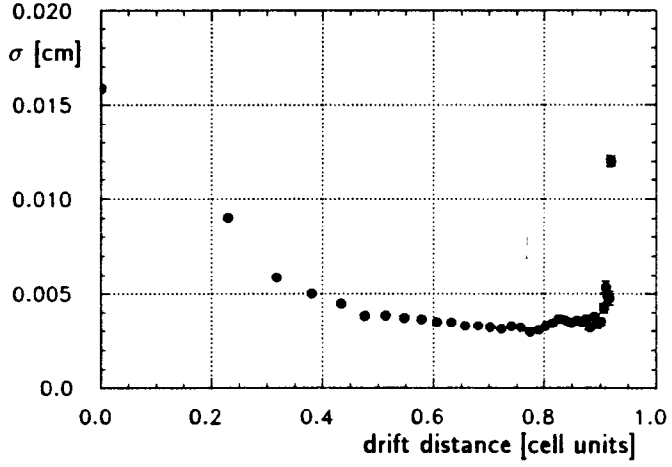

Figure 17: Spatial resolution obtained for CO_2/propane at 3.1 bar (1 cell unit = 2.66 mm).

region of the detector. The obtained spatial resolution for the CO_2/propane mixture is shown in Figure 17.

Due to the missing field-shaping wires there are regions of low electric field between the sense wires where the drift velocity is extremely small (see Figure 16). As a consequence, a reduced efficiency and bad resolution is observed in the outermost 8 % of the drift cell. The resolution deteriorates mainly because the parametrization of the angular correction is not adequate for very large drift distances.

5.4 Background Studies

Since the μVDC is operated very close to the beam line, background investigations are of particular interest. A systematic study was performed using random trigger events. These events are recorded with a frequency of 0.1 Hz, irrespective of any signal from the pretrigger components [1], i.e.,they represent arbitrary bunch crossings. The results of this analysis can be summarized as follows:

- Each bunch crossing produces background hits in the μVDC. The mean number of hits is 30 to 60, depending on the beam conditions. The background is not uniformly distributed in the chamber. The mean occupancy in the innermost sense wire layer was observed to be as high as 20 %, representing a substantial fraction of "blind" wires.

- Only a small fraction of random triggers (typically 1/200) is accompanied by at least one track in the main drift chamber. From this one can conclude that the background from beam-wall events is negligible. The major contribution to the μVDC current is caused by synchrotron radiation photons which enter the chamber with every bunch crossing.

- The observed photon rates are much higher than expected after having modified the bending magnets close to the detector. This indicates that a sizable fraction of the primary radiation does not come from the bends but from beam deflections in the quadrupoles.

- Primary synchrotron radiation from the quadrupoles is not optimally screened by the collimators. In particular it can hit the copper layer on the beryllium beam pipe and induce secondary Cu-K-line emission. In fact these monoenergetic photons (E_γ = 8.05 keV) show up as a broad peak around 180 ADC counts in the measured pulse height spectrum of the background hits (see Figure 18).

As far as the μVDC background rates and currents are concerned, particles from beam-wall interactions can be neglected. However, many of these events

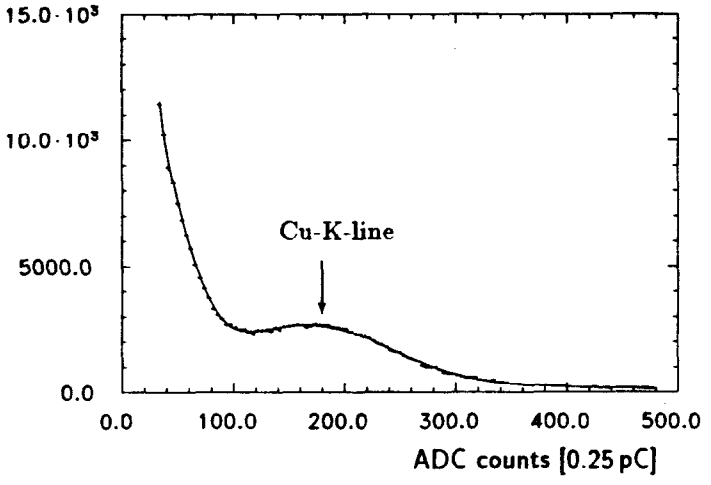

Figure 18: ADC spectrum for random triggers.

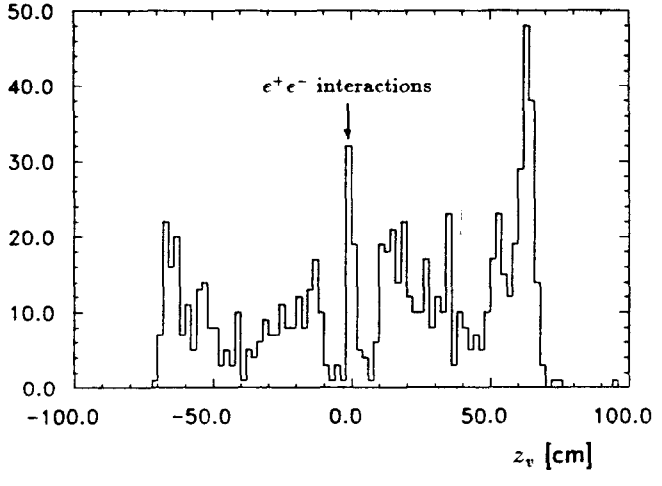

Figure 19: Main vertex positions along the beam line.

are accepted by the trigger and fill the data tapes. In order to find the "hot spots" in the beam pipe region, events from raw data tapes were reconstructed without any cuts applied on the main vertex position. With the old VDC and beam pipe (40 mm inner radius) about 60 % of the events came from beam-wall interactions. As expected, the situation has become much worse with the new narrow beam pipe. For the same trigger conditions there are now 93 % beam-wall events on a raw data tape. Figure 19 shows an enhanced probability for such events in the region of the conical synchrotron radiation scrapers (45 cm $< |z| <$ 70 cm).

Based on the experience just described, a redesigned synchrotron radiation protection scheme will be used for future data taking with the μVDC.

* Current members of the ARGUS Collaboration are: H. Albrecht, H. Ehrlichmann, G. Harder, A. Krüger, R. Mundt, A. Nau, A. W. Nilsson, A. Nippe, T. Oest, M. Reidenbach, M. Schäfer, W. Schmidt-Parzefall, H. Schröder, H. D. Schulz, F. Sefkow, R. Wurth (DESY Hamburg); R. D. Appuhn, C. Hast, G. Herrera, H. Kolanoski, A. Lange, A. Lindner, R. Mankel, M. Schieber, G. Schweda, B. Spaan, A. Walther, D. Wegener (University of Dortmund); M. Paulini, K. Reim, U. Volland, H. Wegener (University of Erlangen); W. Funk, J. Stiewe, S. Werner (University of Heidelberg); S. Ball, J. C. Gabriel, C. Geyer, A. Hölscher, W. Hofmann, B. Holzer, S. Khan, J. Spengler (MPI Heidelberg); D. I. Britton, C. E. K. Charlesworth, K. W. Edwards, H. Kapitza, P. Krieger, R. Kutschke, D. B. MacFarlane, K. W. McLean, R. S. Orr, J. A. Parsons, P. M. Patel, J. D. Prentice, S. C. Seidel, G. Tsipolitis, K. Tzamariudaki, R. van de Water, T.-S. Yoon (IPP Canada); S. Schael, K. R. Schubert, K. Strahl, R. Waldi, S. Weseler (University of Karlsruhe); B. Boštjančič, G. Kernel, P. Križan, E. Križnič, T. Živko (University of Ljubljana); H. I. Cronström, L. Jönsson (University of Lund); A. Babaev, M. Danilov, A. Droutskoy, B. Fominykh, A. Golutvin, I. Gorelov, V. Lubimov, F. Ratnikov, A. Rostovtsev, A. Semenov, S. Semenov, V. Shevchenko, V. Soloshenko, V. Tchistilin, I. Tichomirov, Yu. Zaitsev (ITEP Moscow); R. Childers, C. W. Darden (University of South Carolina).

References

[1] H. Albrecht *et al.* (ARGUS Collaboration), Nucl. Instr. Meth. **A275** (1989) 1.

[2] See any recent review of B physics, for example
H. Schröder, Physics of B Mesons, DESY preprint DESY 88-101, July 1988;
S. Stone, The Quark Mixing Matrix, Charm Decays and B Decays, *CP Violation*, ed. C. Jarlskog, World Scientific Publishing Co., Singapore, 1989.

[3] See for example C. Jarlskog, Z. Phys. **C29** (1986) 491.

[4] R. Fulton *et al.* (CLEO Collaboration), Phys. Rev. Lett. **64** (1990) 16.

[5] H. Albrecht *et al.* (ARGUS Collaboration), Phys. Lett. **234B** (1990) 409.

[6] G. Altarelli *et al.*, Nucl. Phys. **B208** (1982) 365.

[7] M. Wirbel *et al.*, Z. Phys. **C29** (1985) 637.

[8] J. G. Körner and G. A. Schuler, Z. Phys. **C38** (1988) 511.

[9] B. Grinstein *et al.*, Phys. Rev. Lett. **55** (1986) 298;
N. Isgur *et al.*, Phys. Rev. **D39** (1989) 799.

[10] H. Albrecht *et al.* (ARGUS Collaboration), Exclusive Hadronic Decays of *B* Mesons, DESY preprint DESY 90-046, May 1990.

[11] Particle Data Group, Review of Particle Properties, Phys. Lett. **B204** (1988) 1.

[12] P. Avery *et al.* (CLEO Collaboration), Phys. Lett. **223B** (1989) 470;
H. Albrecht *et al.* (ARGUS Collaboration), Search for $b \to s\,gluon$ in *B* Meson Decays, DESY preprint DESY 89-096, August 1989.

[13] L. Michel, Proc. Phys. Soc. **A63** (1950) 514;
C. Bouchiat and L. Michel, Phys. Rev. **106** (1957) 170.

[14] W. Bacino *et al.* (DELCO Collaboration), Phys. Rev. Lett. **42** (1979) 749.

[15] S. Behrends *et al.* (CLEO Collaboration), Phys. Rev. **D32** (1985) 2468.

[16] W. T. Ford *et al.* (MAC Collaboration), Phys. Rev. **D36** (1987) 1971.

[17] H. Janssen *et al.* (Crystal Ball Collaboration), Phys. Lett. **B228** (1989) 273.

[18] H. Albrecht *et al.* (ARGUS Collaboration), Determination of the Michel Parameter in Tau Decay, DESY preprint DESY 90-059, May 1990 (to be published in Phys. Lett. **B**).

[19] A. Ali and Z. Z. Aydin, Nuovo Cimento **A43** (1978) 270.

[20] J. H. Kühn and F. Wagner, Nucl. Phys. **B236** (1984) 16.

[21] J. H. Kühn and A. Santamaria, τ Decays to Pions, MPI Munich preprint MPI-PAE/PTh 17/90, April 1990.

[22] H. Albrecht *et al.* (ARGUS Collaboration), Determination of the Tau-Neutrino Helicity, DESY preprint DESY 90-079, July 1990 (to be published in Phys. Lett. **B**).

[23] H. Albrecht *et al.* (ARGUS Collaboration), Z. Phys. **C33** (1986) 7.

[24] K. W. Edwards *et al.*, Nucl. Instr. Meth. **A252** (1986) 384.

[25] E. Michel *et al.*, Nucl. Instr. Meth. **A283** (1989) 544.

[26] J. Va'vra, Aging of Gaseous Detectors, SLAC-PUB-5207, March 1990.